SAND2023-13025J

Molten Sodium Penetration in NaSICON Electrolytes at 0.1 A cm^{-2}

Ryan Hill,[a] Amanda Peretti,[b] Leo J. Small,[b] Erik D. Spoerke,[b] and Yang-Tse Cheng[a]*

a. Department of Chemical and Materials Engineering, University of Kentucky, Lexington, KY, 40506, USA.

b. Sandia National Laboratories, Albuquerque, NM, 87123, USA

Keywords: sodium batteries, solid electrolytes, dendrites, NaSICON, electrochemistry

Abstract

High conductivity solid electrolytes, such as the Na super ion conductor, NaSICON, are poised to play an increasingly important role in safe, reliable battery-based energy storage, enabling advanced sodium-based batteries. Coupled demands of increased current density (≥0.1 A cm^{-2}) and low temperature (<200 °C) operation, combined with increased discharge times for long duration storage (>12 h), challenge the limitations of solid electrolytes. Here, we explore the penetration of molten sodium into NaSICON at high current densities. Previous studies of β''-alumina proposed that Poiseuille pressure-driven cracking (Mode I) and recombination of ions and electrons within the solid electrolyte (Mode II) are the two main mechanisms for Na penetration, but a comprehensive study of Na penetration in NaSICON is necessary, particularly at high current

density. To further understand these modes, this work employs unidirectional galvanostatic testing of Na|NaSICON|Na symmetric cells at 0.1 A cm^{-2} over 23 hours at 110 °C. While galvanostatic testing shows a relatively constant, yet increasingly noisy voltage profile, electrochemical impedance spectroscopy (EIS) reveals a significant decrease in cell impedance correlated with significant sodium penetration, as observed in scanning electron microscopy (SEM). Further SEM analysis of sodium accumulation within NaSICON suggests that Mode II failure may be far more prevalent than previously considered. Further, these findings suggest that total (dis)charge density (mAh cm^{-2}), as opposed to current density (mA cm^{-2}), may be a more critical parameter when examining solid electrolyte failure, highlighting the challenge of achieving long discharge times in batteries using solid electrolytes. Together, these results provide a better understanding of the limitations of NaSICON solid electrolytes under high current and emphasize the need for improved electrode-electrolyte interfaces.

1. Introduction

Sodium (Na) batteries have recently generated excitement for grid-scale energy storage.[1-4] Particularly, batteries that employ solid or liquid Na metal electrodes benefit from their extremely high theoretical specific capacity (1166 mAh g^{-1}), low reduction potential (-2.71 V vs. standard hydrogen electrode), and earth abundance.[5-13] However, solid Na metal does not form a highly stable solid electrolyte interphase (SEI) in the presence of liquid electrolytes, leading to continuous capacity degradation.[14-16] This drawback has motivated the use of solid electrolytes, such as NaSICON ($Na_{1+x}Zr_2Si_xP_{3-x}O_{12}$, $0 < x < 3$) and β”-alumina, that are stable in the presence of Na metal and can serve as a conduction pathway for Na^+.[17-19] Additionally, it was originally believed that solid electrolytes would eliminate the issue of dendrite formation that plagues solid Na metal

electrodes, due to their high mechanical strength.[20] This expectation, however, has been disproven as dendrites still form easily within solid electrolytes above a critical current density (CCD) (typically ~ 1 mA cm^{-2} at room temperature).[21-27] Dendrite formation can be alleviated by employing molten Na metal as an electrode, such as in Na-S and ZEBRA batteries. This improvement is due to the increased conductivity of the solid electrolyte and better wetting of molten Na metal on the electrolyte surface at elevated temperatures (which reduces the interfacial resistance).[28-32] Despite these improvements, dendrites still form at sufficiently high current densities, limiting the high-current performance of these batteries.[33-37] Here, we seek to understand the mechanisms for Na dendrite formation in the highly conductive Na-ion conductor, NaSICON, which is recognized as a promising solid-state conductor, particularly for lower-temperature molten Na battery applications.[8-11, 17, 19, 32, 38-40]

The mechanisms driving dendrite initiation and propagation from either solid or liquid metal electrodes are not fully understood. In the solid metal electrode case, it is believed that voids form at the electrode-electrolyte interface during stripping due to insufficient metal replenishment by diffusion or creep. These voids lead to an increased local current density at the remaining electrode-electrolyte interface during plating and these areas with high local current density preferentially plate metal (i.e., dendrites).[21, 22, 41-43] In the case of liquid electrodes, it has been suggested that liquid metal can fill existing defects, pores, and microcracks at the surface of solid electrolytes. During plating, additional liquid metal is filled into these features and Poiseuille pressure is generated. If the stress induced by this pressure exceeds a critical value (i.e., fracture toughness of the electrolyte) Na filled cracks can propagate through the entirety of the solid electrolyte. The high pressures are typically induced at much higher current densities (>10 mA cm^{-2}) than the ~ 1 mA cm^{-2} CCD observed in all-solid-state batteries.[34, 36, 37] This mechanism has

previously been referred to as Mode I failure in solid electrolytes exposed to liquid metal electrodes.[34] In the case of both solid and liquid metal electrodes, recombination of the mobile cations with electrons within the electrolyte can lead to internal metal plating. The internally plated metal can serve as sites for further Na^+ and electron recombination and extend throughout the electrolyte. This mechanism has been referred to as Mode II failure in solid electrolytes exposed to solid or liquid metal electrodes. [34, 35, 43, 44]

Characterizing these systems to clearly identify dendrite formation mechanisms in solid electrolytes presents significant challenges. As opposed to liquid electrolytes, solid electrolytes block dendrites from view in many *in situ* imaging techniques. Sakamoto, *et al*. have imaged dendrite formation from liquid Li in garnet electrolytes in real-time from an in-plane configuration and suggested that a build-up of pressure from excessively high current densities (particularly at existing defects) drives metal penetration.[45] Multiple groups have performed *in situ* and *ex situ* imaging of metal penetration in solid electrolytes from solid Na and Li electrodes.[22, 23, 46-48] X-ray computed microtomography (μCT) and other non-destructive imaging techniques have recently proven useful in probing dendrite formation from solid metal electrodes without disassembling the battery or damaging the electrolyte.[49, 50] However, to the best of our knowledge, similar studies examining metal penetration in NaSICON from liquid Na have not yet been published.

The present work combines electrochemical measurements and *ex situ* characterization techniques to probe metal penetration and shorting behavior in cells with liquid Na electrodes. NaSICON is used as the solid electrolyte in liquid Na symmetric cells and exposed to unidirectional current for up to 23 hours. Scanning electron microscopy (SEM) imaging is employed to observe the formation and progression of dendrites after testing. Our findings suggest that Mode II failure is a major contributor to the formation of dendrites within NaSICON and that (dis)charge density

(mAh cm^{-2}) may be just as important as current density (mA cm^{-2}) when considering electrolyte damage and failure. These conclusions can guide the design of solid electrolytes for use in molten sodium batteries, particularly those employed for long duration storage.

2. Experimental

NaSICON Preparation

NaSICON is a fast Na^+ conductor discovered by Hong and Goodenough in 1976.[17] Na^+ is transported through the bottlenecks created by corner-sharing zirconia octahedra and silica tetrahedra.[51, 52] NaSICON synthesis was achieved using solid-state ceramic processing techniques described by Gross *et al*.[53] $ZrSiO_4$ (Sigma-Aldrich, -325 mesh) and $Na_3PO_4 \cdot 12H_2O$ (Sigma-Aldrich, >98%), SiO_2 (Sigma-Aldrich) and $NaCO_3$ (Fisher Scientific) powders were ball-milled in ethanol in a 2:0.6:0.4:0.8 molar ratio and subsequently dried by rotary evaporation before further drying under vacuum overnight. The resulting NaSICON precursor powder was calcined at 600 °C for 12 h in air. Calcined powder was passed through a 150 μm sieve and uniaxially pressed in a 1-1/8" die to 20,000 psi, followed by isopressing to 30,000 psi. The pressed cylinder was sintered on a bed of NaSICON precursor powder, covered with a crucible and heated in air at 5 °C min^{-1} to 1230 °C, including holds at 400 °C for 2 h and 600°C for 4 h. The sample was then held at 1230 °C for 12 h before cooling to room temperature at 5 °C min^{-1}. After sintering, the cylinder was sliced into approximately 1 mm thick discs (~1" diameter) using a Buehler Isomet High Speed Pro saw and polished on both sides to 4000 grit. Chemical analysis of NaSICON via inductively coupled plasma and LECO O (NSL Analytical, Cleveland, OH) yielded a composition of $Na_{3.38}Zr_{1.92}Si_{2.56}P_{0.64}O_{12}$, in line with the target composition $Na_{3.4}Zr_{2.0}Si_{2.4}P_{0.6}O_{12}$. Density by Archimedes method was 96-98% of theoretical density. Phase purity, as evaluated by x-ray

diffraction shown in **Figure S1**, revealed only the desired NaSICON phase (PDF# 04-022-0983) and trace m-$ZrSiO_4$ (PDF# 04-021-7113).

Symmetric Cell Assembly and Electrochemical Testing

Na|NaSICON|Na symmetric cells were assembled inside an argon-filled glovebox (H_2O and O_2 levels <0.1 ppm). Molten Na (99.8%, Thermo Scientific Chemicals) was pipetted into two glass tubes with tungsten rod current collectors glass sealed at the end opposite the opening. Ethylene propylene diene monomer rubber (EPDM) o-rings were fitted on each glass tube and the NaSICON pellet was placed between the two o-rings. The glass tubes were then clamped together to complete the cell assembly. Gross *et al*. used similar cells in a previous work and a schematic is included in **Figure S2**.[53] The Na|NaSICON contact area was 1.77 cm^2. The cells were transferred to a homemade oven with electrical connections within the glovebox. The oven temperature was set at 110 ± 1 °C to keep the Na electrodes molten.

Electrochemical testing was performed using a Solartron 1280C electrochemical test station and electrochemical impedance spectroscopy was performed using an HP 4194A impedance analyzer. Galvanostatic tests were performed by applying 100 mA cm^{-2} current in one direction. Current was applied in one direction to differentiate the behavior at the plating and stripping side of the electrolyte. Current was applied to the cells for either 1 hour or 23 hours to observe the time dependence of current-induced damage. Galvanostatic current was applied in 1-hour intervals and impedance spectra were obtained before the first interval, and after each subsequent interval. Impedance spectra were collected at the open circuit potential by applying a 10 mV sinusoidal voltage over the range of 1 MHz – 100 Hz. Spectra were fitted to an equivalent circuit using EC-Lab's Z-Fit function. Samples are named as NaSICON-Xh, where X defines the number of total

hours (h) current was applied to the corresponding symmetric cell. Before symmetric cell testing, the pellets were sputtered with gold blocking electrodes and the ionic and electronic conductivity were measured by AC and DC polarization, respectively. It was found that the ionic conductivity at room temperature was 3.1 mS cm^{-1} and the electronic conductivity was 2.0 x 10^{-6} mS cm^{-1}, implying a transference number of approximately 1.

Imaging

Surface and cross-sectional images were obtained using an FEI Quanta 250 field emission SEM. Cross-sections of the NaSICON samples were prepared by breaking the pellets inside of an Ar-filled glovebox. Samples were only briefly exposed to air before transfer to the SEM. Images and EDS maps were acquired using an accelerating voltage of 15 kV. Samples were imaged before and after electrochemical tests to determine the effect of current on the pellets' microstructure.

3. Results and Discussion

Symmetric Cell Testing

Two cells were tested, NaSICON-1h and NaSICON-23h, for 1 h and 23 h, respectively. The final pellet thickness for each cell was 0.80 mm for the NaSICON-1h cell and 0.75 mm for the NaSICON-23h cell. The voltage profiles and EIS spectra of the Na|NaSICON|Na symmetric cells are shown in **Figure 1**. EIS spectra were fitted to the equivalent circuit shown in the inset in **Figure 1b**. All fitted values are included in **Table S1** and **Table S2**. As shown in the inset of **Figure 1a**, the overpotential response of both cells during the first hour is very similar. Both cells exhibit an initial voltage drop and subsequent plateau that likely represent improved wetting of Na on NaSICON upon application of current. From the EIS spectra in **Figure 1b**, it is seen that the total

resistance of the NaSICON-1h cell drops from 18.8 to 12.3 Ω, as measured by the sum of the two x-axis intercepts, after testing. The NaSICON-23h cell exhibits a similar drop (**Figure 1c**) after

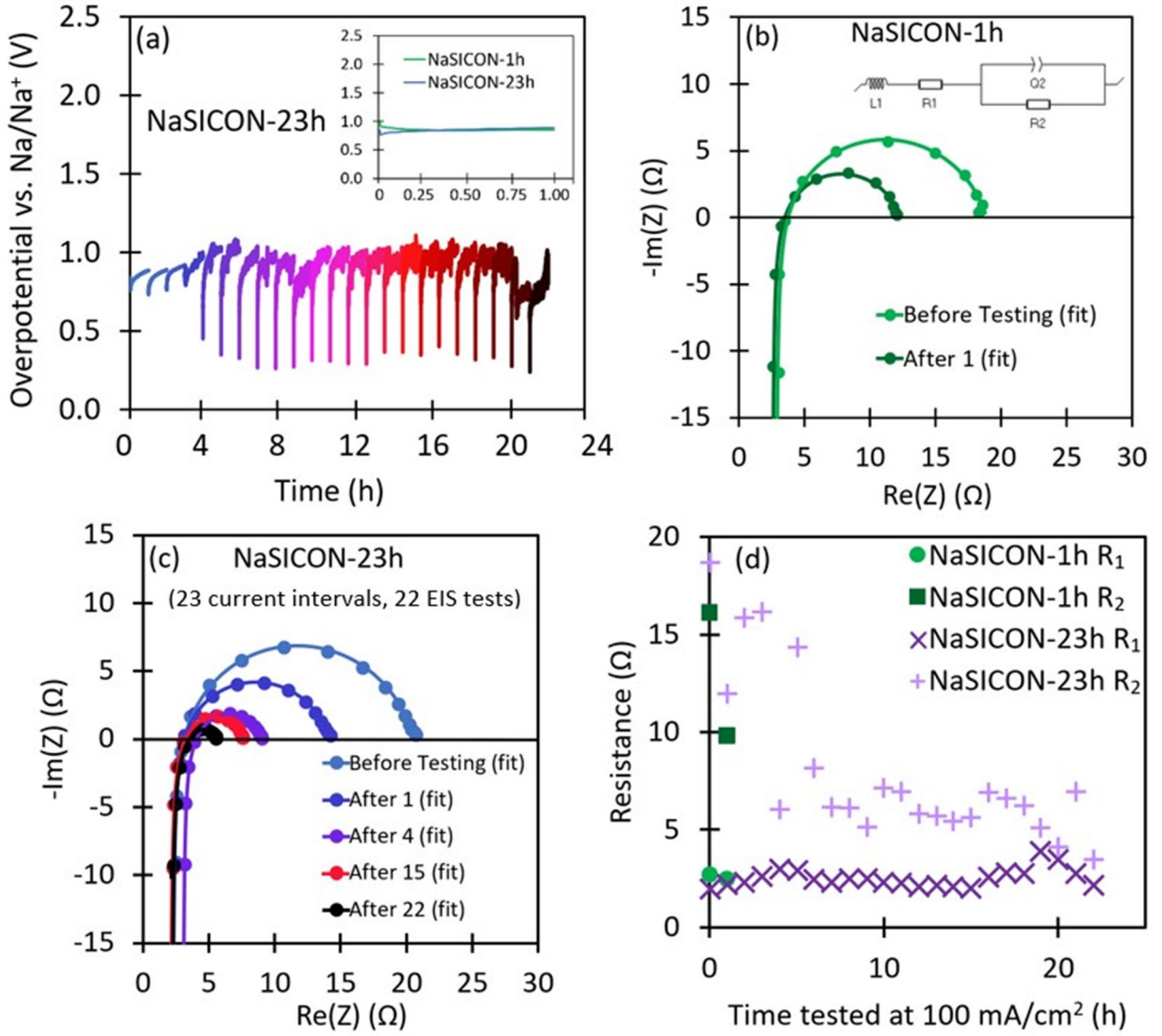

Figure 1. (a) Voltage profiles and (b & c) EIS spectra of Na|NaSICON|Na symmetric cells. (d) Values of R_1 and R_2 measured by EIS as symmetric cells are tested. Inset in (a) compares first current interval of NaSICON-1h and NaSICON-23h cells. Inset in (b) shows equivalent circuit used for fitting EIS spectra. Legend entries in (b & c) indicate when each spectrum was collected. For (c-d) only 22 EIS spectra and resistance values were collected for the NaSICON-23h sample, due to Na depletion on one side of the cell after the 23rd interval.

the first DC current interval, dropping from 18.7 to 11.9 Ω. The first x-intercept, R_1, in the EIS spectra has been attributed mainly to the bulk conductivity of the NaSICON electrolyte, but also contains the series resistance from the Na electrodes and tungsten current collectors. This value remains relatively constant near 2.5 Ω throughout testing and appears to determine the plateau voltage during the current intervals, according to Ohm's Law. The decrease in total resistance is almost entirely due to the decrease in R_2. We hypothesize that R_2 is due to interfacial resistance, as it is typically impossible to resolve both bulk grain and grain boundary resistances at this temperature.[54] The decrease in the interfacial resistance is likely the result of improved wetting and increased contact area due to Na penetration of the electrolyte. Previous works have also observed reductions in resistance of Na symmetric cells (with either solid or liquid Na electrodes) or improved battery performance upon application of current or by introducing a coating that facilitates Na wetting.[38, 46, 53, 55] The complete R_1 and R_2 behavior for each cell is shown in **Figure 1d**.

The voltage response in the NaSICON-23h cell (**Figure 1a**) is slightly different from the NaSICON-1h sample, in that it displays an "arc-and-plateau" feature during the intervals. Both cells show an initial voltage drop attributed to improved wetting upon applying current. However, the overpotential in the NaSICON-1h cell then slowly decays to a plateau, whereas the overpotential in the NaSICON-23h cell arcs to a nearly identical plateau, as determined by the R_1 value. The first four intervals in the NaSICON-23h cell display this arc-and-plateau pattern, with the overpotential becoming somewhat noisy near the end of the fourth interval. During the 5^{th}-21^{st} intervals, the initial measured overpotential is consistently low (< 0.5 V) before quickly increasing and eventually plateauing near ~ 1 V. Then, during the 22^{nd} interval, the overpotential displays a short plateau near 0.9 V before dropping and showing another plateau near 0.7 V. Finally, in the

23rd interval, the overpotential begins low at 0.24 V, plateaus near 0.75 V, and then increases rapidly near the end of the interval. The increase at the end of the 23rd interval represents disconnection of the liquid Na electrode from the tungsten rod current collector as the level of the liquid Na reservoir became too low and the test could not be continued.

The shape of the profile in the 1st to 22nd intervals (**Figure 1a**) could provide insight to the processes occurring in the NaSICON-23h sample. The arc-and-plateau feature has previously been observed in Li symmetric cells with liquid electrolyte and was studied in depth by Chen *et al*. who found that the arc-and-plateau feature is due to mass transport behavior through the bulk carbonate liquid electrolyte as well as through a tortuous dead Li layer at the Li|electrolyte interface.[56] The tortuous dead Li layer can impede Li^+ transport, resulting in drastic concentration gradients near the electrode|electrolyte interface that are necessary to maintain the applied current. These gradients may not reach steady state during the applied current interval, resulting in the continuously rising overpotential. The high applied current density in this study is likely sufficient to establish similarly drastic concentration gradients and the gradients near the Na|NaSICON interfaces are likely much different than within the bulk electrolyte. Additionally, as significant amounts of Na are stripped from one side of the electrolyte, voids may nucleate at the Na|NaSICON interface (as Na does not wet NaSICON well at 110 °C),[53] causing a slight reduction in contact area and corresponding increase in overpotential. In this work, it appears that the voltage eventually approaches its steady state as the plateau becomes nearly flat at the end of the interval. This formation of voids at the electrode|electrolyte interface could also be a possible explanation for the noisy overpotential that is observed during the 4th-23rd intervals.

The EIS spectra in **Figure 1c** and resistance values in **Figure 1d** provide additional insight to the behavior of the NaSICON-23h cell. After the initial drop, the value of R_2 then stabilizes to an

approximately constant value after the second and third intervals, implying steady current-voltage behavior. During the fourth current interval, however, the overpotential profile becomes somewhat noisy. EIS reveals that the total resistance significantly decreases from 16. 2 to 6.0 Ω after the fourth interval. This resistance drop coincides with the initially low and noisy voltage response during the 5th interval and is likely indicative of Na beginning to short the electrolyte. The initial overpotential is much lower than that observed in previous intervals and is too low to be attributed to conduction purely through NaSICON. Additionally, noisy voltage profiles in Li-ion cells have been attributed to so-called "soft shorts" where small regions of the cell become shorted, but the high current density passed through the shorted area causes the accumulated metal to become disconnected, either within itself or from the bulk electrode.[57] This soft short can re-establish itself many times and result in a noisy voltage profile, such as that observed in the 5th-21st intervals. The voltage profile maintains a similar shape through the 21st interval, and the value of R_2 remains between 4-8 Ω. Then, after the 22nd interval, during which a new, lower voltage plateau was observed, R_2 decreases to its lowest value of 3.5 Ω, likely indicating further Na penetration.

Plan-view and cross-sectional Images

Representative plan-view and cross-sectional images of pristine (as-made) NaSICON are shown in **Figure 2a-b**. Additional SEM images of the pristine NaSICON pellets are provided in **Figure S3**. Some porosity and voids can be seen in the untested pellets in both the plan-view and cross-sectional images; however, the images show that the untested pellets are free of any gross internal defects that one might expect to serve as preferential failure sites. There is a very thin dark layer at the surface of the pellet visible in the untested cross-section (**Figure 2b**) that results from polishing. The SEM images in **Figure 2c-f** show plan-view and cross-sectional images of NaSICON after electrochemical testing for 1 or 23 hours. These images provide evidence of the

Na penetration responsible for the resistance decrease described in **Figure 1**. In the pristine cross-section in **Figure 2b**, one consistent microstructure comprising joined cube-like grains, is observed and represents that of NaSICON.[9] In **Figure 2c**, however, a region of the NaSICON sample near the plating side (top of the image) has become darkened but still mostly maintains the cube-like morphology of the pristine NaSICON. This morphology is believed to reflect the earliest stages of Na penetration within the electrolyte, where Na has begun to enter the pellet and the darkening may be due to Na penetrating along grain boundaries. Grain boundaries in solid electrolytes have previously been considered as sites for preferential metal penetration and, in this case, the small voids observed in the plan-view image in **Figure 2a** could allow the liquid electrodes facile access to exposed grain boundaries.[58-60] These voids could then serve as the initial pathways for Na to infiltrate NaSICON, increasing the true contact area and decreasing the total resistance. Further, in **Figure 2d**, a small region of the electrolyte is penetrated by Na metal on the stripping side (bottom of the image) and the dark region is confirmed as bulk Na metal by the EDS map in **Figure 3a**. The dark region in **Figure 3a** clearly shows an intense Na signal compared to the unaffected region of the image and the accompanying reduced Si signal indicates that this region is mostly pure Na metal (that likely partially reacted with O upon transfer to the SEM chamber). The EDS spectrum showing all relevant elements for **Figure 3a** is included in **Figure S4**. This penetration of Na provides a pathway with increased conductivity and could significantly reduce the total resistance observed by EIS. Interestingly, this penetration from the stripping side electrode contradicts the classical thought that Mode I (pressure-induced cracking from the plating side) causes most of the metal accumulation in solid electrolytes. Due to Na predominantly accumulating on the stripping side, we suggest that Mode II (recombination of ions and electrons

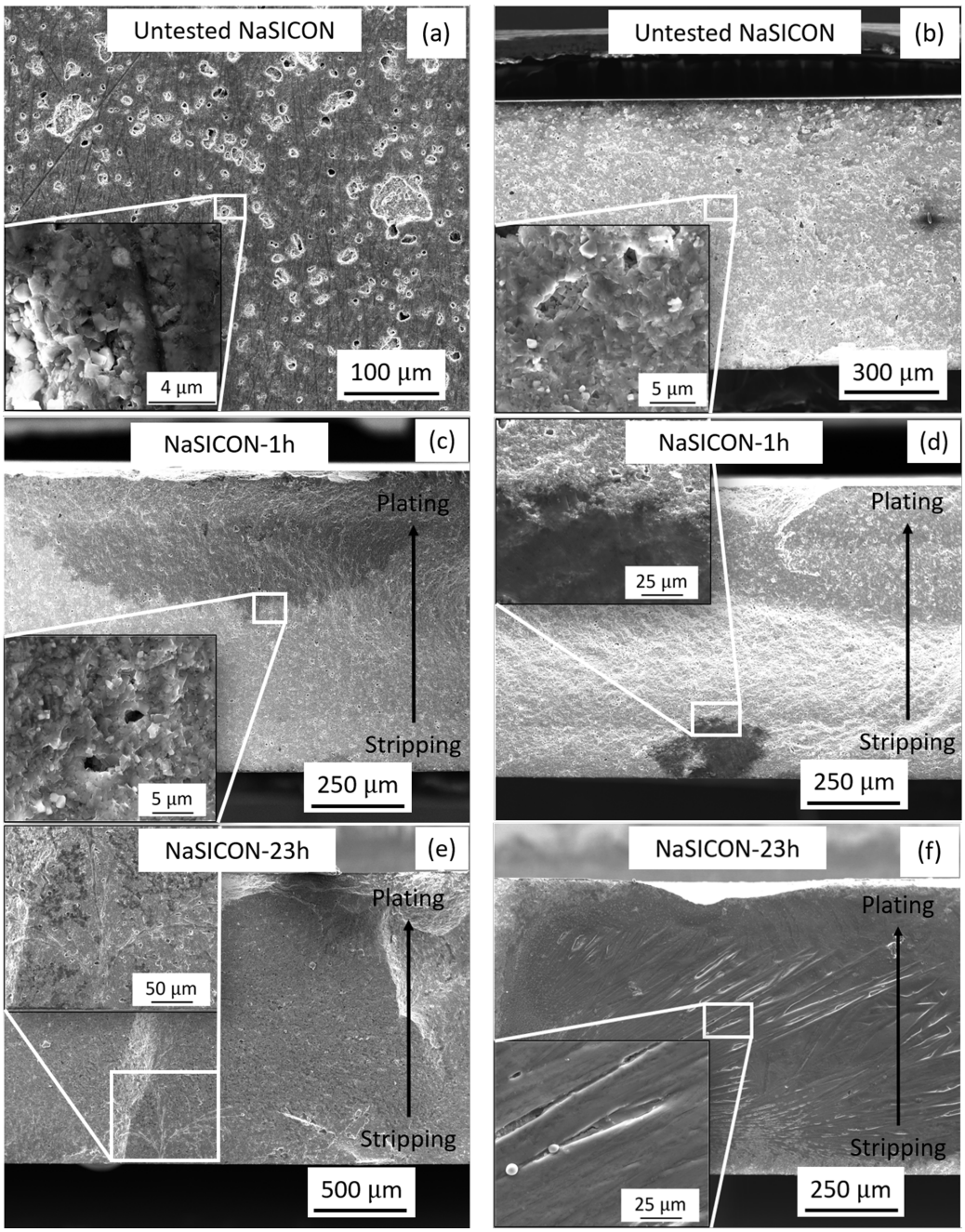

Figure 2. Planview (a) and cross-sectional (b) SEM images of pristine NaSICON. (c-f) Cross-sectional SEM images of electrochemically tested NaSICON. (c & d) NaSICON-1h sample after testing. (e & f) NaSICON-23h sample after testing. Inset in each image shows a higher magnification image of the boxed region. The top of the images (c-f) corresponds to the plating side of the electrolyte and the bottom of the images corresponds to the stripping side.

in the electrolyte interior) caused this accumulation and could be more prevalent in the failure of solid electrolytes than previously suspected. It is important to note that Na accumulation still occurred, albeit far less, on the plating side (Mode I) of the electrolyte in the NaSICON-1h cell and a representative SEM image is shown in **Figure S5**. Additionally, the darkened NaSICON-like region in **Figure 2c** does not exhibit increased Na signal in EDS maps and we believe the concentration of Na is not increased enough by grain boundary penetration to be visualized by EDS.

Upon examination of the cross-section of the NaSICON-23h sample (**Figure 2e-f** and **Figure 3b**), significant amounts of Na metal have clearly accumulated within the electrolyte, extending across the entire thickness. The EDS spectrum showing all relevant elements for **Figure 3b** is shown in **Figure S4**. These spectra show that the NaSICON-23h pellet has a much higher relative amount of sodium in the cross-section, which is also clear in the SEM images. Interestingly, it does not appear that current passes through only the Na metal pathways even when completely shorted, as the plateau voltage in the 5^{th}-22^{nd} intervals remains near 1.0 V, which would be expected for non-shorted ionic conduction through NaSICON. The cell also fails due to Na depletion at the stripping electrode, confirming some Na^+ conduction occurred during the later intervals. Again, this observation may be explained by the soft shorting phenomenon. Shorting can be confirmed, however, by comparing the true vs. theoretical mass of Na transported. Based on the applied current after 23 1-hour intervals, 3.5 g of Na should have been transferred from the stripping to plating electrode. Upon measuring the mass of Na on either side of the cell, though, it was found that only 2.3 g of Na had been transported, corresponding to a transfer efficiency of 65.7 %. The low efficiency implies that there was an additional pathway for current to pass through the cell and the most likely candidate was electronic conduction through Na metal that had penetrated the

thickness of the solid electrolyte. This pathway was most likely initially established sometime during the fourth current interval, when the voltage profile first became noisy, and may have been exacerbated during the 22nd interval, when the overpotential dropped to a lower plateau value. However, even though Na has penetrated much of the cross-section in the NaSICON-23h sample, the total resistance is not low enough to be attributed purely to Na, which has an electronic conductivity of 1.0 x 10^5 S cm^{-1} at 110 °C.[61] The higher resistance and maintained Na^+ transport would support the conclusion that current does not pass entirely through these Na-penetrated regions, but instead that the Na creates new, higher conductivity pathways and increases contact between Na and NaSICON, lowering the total resistance of the electrolyte.

In **Figure 2e**, the observed Na penetration appears as a branched structure that begins from a single

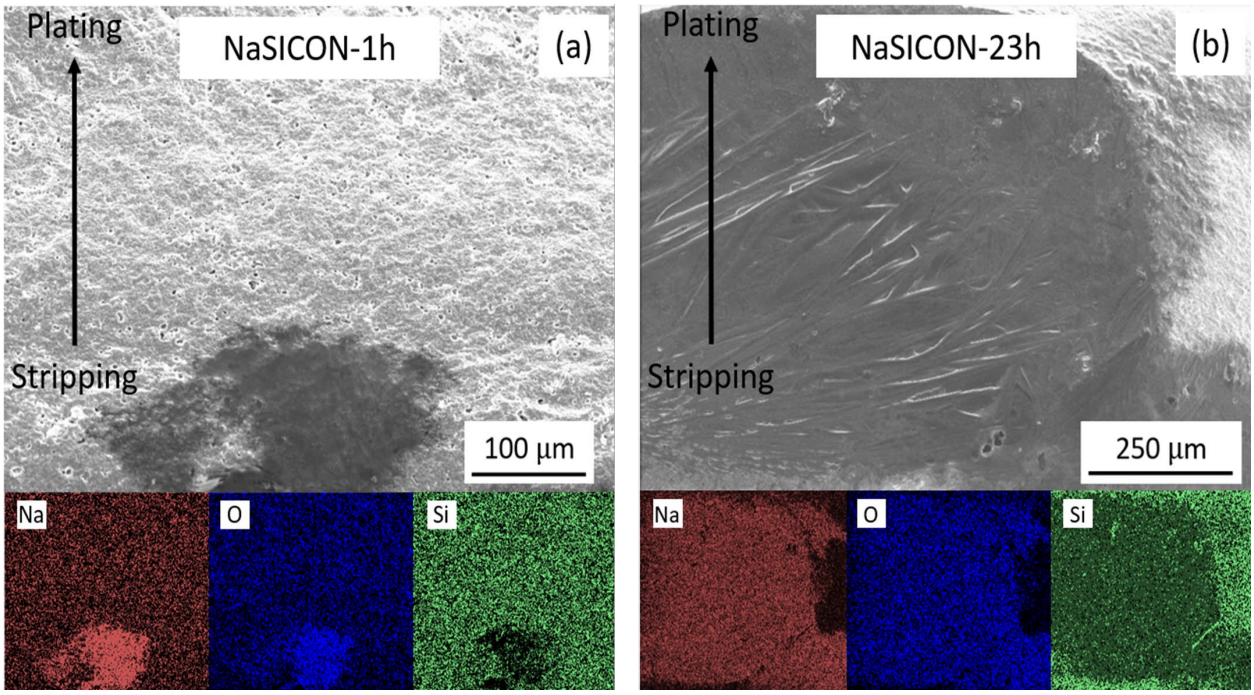

Figure 3. Cross-sectional SEM images and corresponding sodium, oxygen, and silicon EDS maps of tested NaSICON samples. (a) NaSICON-1h sample. (b) NaSICON-23h sample. The top of the images corresponds to the plating side of the electrolyte and the bottom of the images corresponds to the stripping side.

point on the stripping side of the electrolyte, reminiscent of the typical dendrite structure from solid metal anodes.[22, 23, 62] An EDS map of this image is included in **Figure S6** that confirms this structure having a high concentration of Na, indicating the presence of Na metal. Again, this penetration begins from the stripping side of the electrolyte and would imply that Mode II is responsible for significant metal formation in the electrolyte. The substantial Mode II metal formation seen in these cells may have been exacerbated by the fact that half of the electrolyte in a symmetric cell is exposed to potentials favorable for metal plating, leading to plating deeper within the electrolyte than previously expected, particularly if pores and other defects exist (as they do for all sintered solid electrolytes).[63] **Figure 2f**, depicting another region of the cross-section from the NaSICON-23h sample, also appears to show lines of Na metal that extend from the stripping to plating side of the electrolyte, but it is not clear if these lines indicate initiation from the stripping side.

The regions with significant metal accumulation are also regions where current is likely concentrated due to improved Na wetting on the NaSICON surface, explaining why the entire surface does not display this color and microstructure. This improved wetting (whether it results from early Na penetration or is purely due to surface features) would lower the local resistance. The lower local resistance would likely cause high localized current, giving a higher chance of Na^+ and electron recombination within the electrolyte (Mode II), and, eventually, Na accumulation. The progression of Na accumulation observed in these cross-sections is surprising when the classical idea of critical current density is considered. Previous literature has suggested that at high enough current density, solid electrolytes will quickly fail due to the formation of dendrites.[21, 24, 34, 36] Our observation of progressive failure, however, suggests that while some metal formation may occur quickly, it is more appropriate to consider both current density *and*

(dis)charge time when examining electrolyte failure. The combination of the two parameters would suggest a critical charge density should be considered, rather than just a critical current density. We suspect metal may penetrate these electrolytes even at lower current densities, but the effects are not prevalent until sufficient charge per unit area has passed – such as in the NaSICON-23h cell where the electrolyte passed 2.3 Ah cm^{-2}. Since most papers focus on cycling (as opposed to unidirectional current), small metal accumulations within the electrolyte could be stripped away when the polarity of the cell is reversed, making the earliest metal formation difficult to detect. This further consideration of discharge time when examining solid electrolyte failure will be especially important for the progress of stationary, long duration storage, where discharge times of > 12 h are desired.

4. Conclusions

NaSICON solid electrolytes were synthesized and tested in liquid Na symmetric cells to study the Na|NaSICON interface and the propagation of Na metal through the solid electrolytes. A unidirectional current density of 100 mA cm^{-2} was applied to the cells for up to 23 1-hour intervals to probe the early and late stages of Na-electrolyte interaction. We found that:

- The total resistance – and particularly the interfacial resistance - of the symmetric cells decreased with the application of 100 mA cm^{-2} current density.
- The overpotential during testing depended on the bulk ionic conductivity of the electrolyte.
- Na accumulation in NaSICON solid electrolytes appeared to occur in two stages. First Na may have infiltrated grain boundaries from the surface of the electrolyte, appearing as discolored NaSICON. These regions then served as current concentrators and eventually further Na

accumulation occurred until bulk metallic Na was present in the interior of the electrolyte. The progressive accumulation suggests that both a critical current density and critical total charge density are important criteria for solid electrolytes.

- Na accumulation initiated on both the stripping or the plating side of the electrolyte. Previous models stated that most metal accumulation in liquid electrode cells begins on the plating side (due to Poiseuille pressure buildup). Our observations, however, show that discoloration, accumulation of Na metal, and even branching of dendrite-like Na also initiated *at the stripping side* of the electrolyte and may have then extended across the entire thickness. Na accumulation on the stripping side suggests that Mode II may be a significant mechanism just as prevalent as Mode I in NaSICON solid electrolytes at high current densities.

- Local regions on the NaSICON surface with improved Na wetting may also have served as current concentrators that initiated Na accumulation. This phenomenon would be similar to the behavior seen in all-solid-state batteries where regions of the metal electrode in good contact with the electrolyte act as current concentrators and preferentially form dendrites.[21, 64]

These findings help provide a better understanding of the metal plating behavior in solid electrolytes in the presence of liquid metal electrodes. As liquid metal batteries become more important in the field of energy storage, these insights promise to inform the design of improved battery systems.

ASSOCIATED CONTENT

The following files are available free of charge.

XRD spectra of pristine NaSICON, symmetric cell schematic, all fitted values from EIS tests, additional SEM images of pristine and tested NaSICON, and additional EDS spectra/maps of tested NaSICON pellets

AUTHOR INFORMATION

Corresponding Author

Ryan Hill

Department of Chemical and Materials Engineering

University of Kentucky College of Engineering

177 F Paul Anderson Tower

512 Administration Drive

Lexington, KY 40506

Ryan.C.Hill@uky.edu

Author Contributions

The manuscript was written through contributions of all authors. All authors have given approval to the final version of the manuscript.

ACKNOWLEDGMENT

This work was conducted through a collaboration between the University of Kentucky and Sandia National Laboratories and was supported by the Energy Storage Program, managed by Dr. Imre Gyuk, in the U.S. Department of Energy's Office of Electricity. Sandia National Laboratories is a

multimission laboratory managed and operated by National Technology & Engineering Solutions of Sandia, LLC, a wholly owned subsidiary of Honeywell International Inc., for the U.S. Department of Energy's National Nuclear Security Administration under contract DE-NA0003525. This paper describes objective technical results and analysis. Any subjective views or opinions that might be expressed in the paper do not necessarily represent the views of the U.S. Department of Energy or the United States Government.

REFERENCES

(1) Choudhury, S.; Wei, S.; Ozhabes, Y.; Gunceler, D.; Zachman, M. J.; Tu, Z.; Shin, J. H.; Nath, P.; Agrawal, A.; Kourkoutis, L. F.; Arias, T. A.; Archer, L. A. Designing solid-liquid interphases for sodium batteries. *Nat. Commun.* **2017**, *8* (1). DOI: 10.1038/s41467-017-00742-x.

(2) Deng, T.; Ji, X.; Zou, L.; Chiekezi, O.; Cao, L.; Fan, X.; Adebisi, T. R.; Chang, H.-J.; Wang, H.; Li, B.; Li, X.; Wang, C.; Reed, D.; Zhang, J.-G.; Sprenkle, V. L.; Wang, C.; Lu, X. Interfacial-engineering-enabled practical low-temperature sodium metal battery. *Nat. Nanotechnol.* **2022**, *17* (3), 269-277. DOI: 10.1038/s41565-021-01036-6.

(3) Zhang, Z.; Zhang, Q.; Ren, C.; Luo, F.; Ma, Q.; Hu, Y.-S.; Zhou, Z.; Li, H.; Huang, X.; Chen, L. A ceramic/polymer composite solid electrolyte for sodium batteries. *J. Mater. Chem. A* **2016**, *4* (41), 15823-15828. DOI: 10.1039/c6ta07590h.

(4) Li, F.; Wei, Z.; Manthiram, A.; Feng, Y.; Ma, J.; Mai, L. Sodium-based batteries: from critical materials to battery systems. *J. Mater. Chem. A* **2019**, *7* (16), 9406-9431. DOI: 10.1039/c8ta11999f.

(5) Sudworth, J. L. The sodium/nickel chloride (ZEBRA) battery. *J. Power Sources* **2001**, *100*, 149-163. DOI: 10.1016/S0378-7753(01)00891-6.

(6) Seh, Z. W.; Sun, J.; Sun, Y.; Cui, Y. A highly reversible room-temperature sodium metal anode. *ACS Cent. Sci.* **2015**, *1*, 449-455. DOI: 10.1021/ACSCENTSCI.5B00328/ASSET/IMAGES/LARGE/OC-2015-00328H_0004.JPEG.

(7) Ha, S.; Kim, J. K.; Choi, A.; Kim, Y.; Lee, K. T. Sodium–Metal Halide and Sodium–Air Batteries. *Chemphyschem* **2014**, *15*, 1971-1982. DOI: 10.1002/CPHC.201402215.

(8) Gross, M. M.; Percival, S. J.; Lee, R. Y.; Peretti, A. S.; Spoerke, E. D.; Small, L. J. A high-voltage, low-temperature molten sodium battery enabled by metal halide catholyte chemistry. *Cell Rep Phys Sci* **2021**, *2* (7). DOI: ARTN 100489

10.1016/j.xcrp.2021.100489.

(9) Small, L. J.; Eccleston, A.; Lamb, J.; Read, A. C.; Robins, M.; Meaders, T.; Ingersoll, D.; Clem, P. G.; Bhavaraju, S.; Spoerke, E. D. Next generation molten NaI batteries for grid scale energy storage. *J. Power Sources* **2017**, *360*, 569-574. DOI: https://doi.org/10.1016/j.jpowsour.2017.06.038.

(10) Gross, M. M.; Percival, S. J.; Small, L. J.; Lamb, J.; Peretti, A. S.; Spoerke, E. D. Low-Temperature Molten Sodium Batteries. *ACS Applied Energy Materials* **2020**, *3* (11), 11456-11462. DOI: 10.1021/acsaem.0c02385.

(11) Li, G.; Lu, X.; Kim, J. Y.; Meinhardt, K. D.; Chang, H. J.; Canfield, N. L.; Sprenkle, V. L. Advanced intermediate temperature sodium–nickel chloride batteries with ultra-high energy density. *Nat. Commun.* **2016**, *7* (1), 10683. DOI: 10.1038/ncomms10683.

(12) Percival, S. J.; Small, L. J.; Spoerke, E. D. Electrochemistry of the NaI-AlCl3 Molten Salt System for Use as Catholyte in Sodium Metal Batteries. *J. Electrochem. Soc.* **2018**, *165* (14), A3531-A3536. DOI: 10.1149/2.1191814jes.

(13) Wang, Q.; Zhao, C.; Lv, X.; Lu, Y.; Lin, K.; Zhang, S.; Kang, F.; Hu, Y.-S.; Li, B. Stabilizing a sodium-metal battery with the synergy effects of a sodiophilic matrix and fluorine-rich interface. *J. Mater. Chem. A* **2019**, *7* (43), 24857-24867. DOI: 10.1039/c9ta06877e.

(14) Lee, J.; Kim, J.; Kim, S.; Jo, C.; Lee, J. A review on recent approaches for designing the SEI layer on sodium metal anodes. *Mater. Adv.* **2020**, *1*, 3143-3166. DOI: 10.1039/D0MA00695E.

(15) Wang, H.; Matios, E.; Luo, J.; Li, W. Combining theories and experiments to understand the sodium nucleation behavior towards safe sodium metal batteries †. *Chem. Soc. Rev.* **2020**, *49*, 3783. DOI: 10.1039/d0cs00033g.

(16) Mogensen, R.; Brandell, D.; Younesi, R. Solubility of the Solid Electrolyte Interphase (SEI) in Sodium Ion Batteries. *ACS Energy Lett.* **2016**, *1*, 1173-1178. DOI: 10.1021/acsenergylett.6b00491.

(17) Goodenough, J. B.; Hong, H. Y. P.; Kafalas, J. A. Fast Na+-ion transport in skeleton structures. *Mater. Res. Bull.* **1976**, *11*, 203-220. DOI: 10.1016/0025-5408(76)90077-5.

(18) Kummer, J. T. β-Alumina electrolytes. *Prog. Solid State Chem.* **1972**, *7*, 141-175. DOI: 10.1016/0079-6786(72)90007-6.

(19) Li, M. M.; Tripathi, S.; Polikarpov, E.; Canfield, N. L.; Han, K. S.; Weller, J. M.; Buck, E. C.; Engelhard, M. H.; Reed, D. M.; Sprenkle, V. L.; Li, G. Interfacial Engineering with a Nanoparticle-Decorated Porous Carbon Structure on β″-Alumina Solid-State Electrolytes for

Molten Sodium Batteries. *ACS Appl. Mater. Interfaces* **2022**, *14* (22), 25534-25544. DOI: 10.1021/acsami.2c05245.

(20) Monroe, C.; Newman, J. The Impact of Elastic Deformation on Deposition Kinetics at Lithium/Polymer Interfaces. *J. Electrochem. Soc.* **2005**, *152*, A396. DOI: 10.1149/1.1850854.

(21) Kasemchainan, J.; Zekoll, S.; Spencer Jolly, D.; Ning, Z.; Hartley, G. O.; Marrow, J.; Bruce, P. G. Critical stripping current leads to dendrite formation on plating in lithium anode solid electrolyte cells. *Nat. Mater.* **2019**, *18*, 1105-1111. DOI: 10.1038/s41563-019-0438-9.

(22) Golozar, M.; Paolella, A.; Demers, H.; Savoie, S.; Girard, G.; Delaporte, N.; Gauvin, R.; Guerfi, A.; Lorrmann, H.; Zaghib, K. Direct observation of lithium metal dendrites with ceramic solid electrolyte. *Sci. Rep.* **2020**, *10*, 1-11. DOI: 10.1038/s41598-020-75456-0.

(23) Ren, Y.; Shen, Y.; Lin, Y.; Nan, C. W. Direct observation of lithium dendrites inside garnet-type lithium-ion solid electrolyte. *Electrochem. Commun.* **2015**, *57*, 27-30. DOI: 10.1016/J.ELECOM.2015.05.001.

(24) Lu, Y.; Zhao, C. Z.; Yuan, H.; Cheng, X. B.; Huang, J. Q.; Zhang, Q. Critical Current Density in Solid-State Lithium Metal Batteries: Mechanism, Influences, and Strategies. *Adv. Funct. Mater.* **2021**, *31*, 2009925. DOI: 10.1002/adfm.202009925

(25) Jiao, S.; Zheng, J.; Li, Q.; Li, X.; Engelhard, M. H.; Cao, R.; Zhang, J. G.; Xu, W. Behavior of Lithium Metal Anodes under Various Capacity Utilization and High Current Density in Lithium Metal Batteries. *Joule* **2018**, *2*, 110-124. DOI: 10.1016/J.JOULE.2017.10.007.

(26) Sharafi, A.; Meyer, H. M.; Nanda, J.; Wolfenstine, J.; Sakamoto, J. Characterizing the Li–Li7La3Zr2O12 interface stability and kinetics as a function of temperature and current density. *J. Power Sources* **2016**, *302*, 135-139. DOI: 10.1016/J.JPOWSOUR.2015.10.053.

(27) Liu, H.; Cheng, X.-B.; Huang, J.-Q.; Yuan, H.; Lu, Y.; Yan, C.; Zhu, G.-L.; Xu, R.; Zhao, C.-Z.; Hou, L.-P.; He, C.; Kaskel, S.; Zhang, Q. Controlling Dendrite Growth in Solid-State Electrolytes. *ACS Energy Lett.* **2020**. DOI: 10.1021/acsenergylett.9b02660.

(28) Fertig, M. P.; Skadell, K.; Schulz, M.; Dirksen, C.; Adelhelm, P.; Stelter, M. From High- to Low-Temperature: The Revival of Sodium-Beta Alumina for Sodium Solid-State Batteries. *Batteries & Supercaps* **2022**, *5*, e202100131. DOI: 10.1002/BATT.202100131.

(29) Almond, D. P.; West, A. R.; Grant, R. J. Temperature dependence of the a.c. conductivity of Naβ-alumina. *Solid State Commun.* **1982**, *44*, 1277-1280. DOI: 10.1016/0038-1098(82)91103-6.

(30) Bohnke, O.; Ronchetti, S.; Mazza, D. Conductivity measurements on nasicon and nasicon-modified materials. *Solid State Ionics* **1999**, *122*, 127-136. DOI: 10.1016/S0167-2738(99)00062-4.

(31) Viswanathan, L.; Virkar, A. V. Wetting characteristics of sodium on β″-alumina and on nasicon. *J. Mater. Sci.* **1982**, *17*, 753-759. DOI: 10.1007/BF00540372.

(32) Zhou, W.; Li, Y.; Xin, S.; Goodenough, J. B. Rechargeable Sodium All-Solid-State Battery. *ACS Cent. Sci.* **2017**, *3*, 52-57. DOI: 10.1021/ACSCENTSCI.6B00321/ASSET/IMAGES/LARGE/OC-2016-00321V_0005.JPEG.

(33) Richman, R. H.; Tennenhouse, G. J. A Model for Degradation of Ceramic Electrolytes in Na-S Batteries. *J. Am. Ceram. Soc.* **1975**, *58*, 63-67. DOI: 10.1111/J.1151-2916.1975.TB18986.X.

(34) De Jonghe, L. C.; Feldman, L.; Buechele, A. Failure modes of Na-beta alumina. *Solid State Ionics* **1981**, *5*, 267-269. DOI: 10.1016/0167-2738(81)90244-7.

(35) De Jonghe, L. C.; Feldman, L.; Beuchele, A. Slow degradation and electron conduction in sodium/beta-aluminas. *J. Mater. Sci.* **1981**, *16*, 780-786. DOI: 10.1007/BF00552217.

(36) Armstrong, R. D.; Dickinson, T.; Turner, J. The breakdown of β-alumina ceramic electrolyte. *Electrochim. Acta* **1974**, *19*, 187-192. DOI: 10.1016/0013-4686(74)85065-6.

(37) Brennan, M. P. J. The Failure of Beta-Alumina Electrolytes by a Dendritic Penetration Mechanism. *Electrochim. Acta* **1980**, *25*, 621-627.

(38) Chang, H. J.; Lu, X.; Bonnett, J. F.; Canfield, N. L.; Han, K.; Engelhard, M. H.; Jung, K.; Sprenkle, V. L.; Li, G. Decorating β″-alumina solid-state electrolytes with micron Pb spherical particles for improving Na wettability at lower temperatures. *J. Mater. Chem. A* **2018**, *6*, 19703-19711. DOI: 10.1039/C8TA06745G.

(39) Kim, J.; Jo, S. H.; Bhavaraju, S.; Eccleston, A.; Kang, S. O. Low temperature performance of sodium–nickel chloride batteries with NaSICON solid electrolyte. *J. Electroanal. Chem.* **2015**, *759*, 201-206. DOI: https://doi.org/10.1016/j.jelechem.2015.11.022.

(40) Bhavaraju, S. Novel Sodium – Polysulfide Flow Battery Grid-scale Energy Storage Technology. In *Electrical Energy Storage Applications and Technologies*, Austin, TX, 2022; EESAT.

(41) Porz, L.; Swamy, T.; Sheldon, B. W.; Rettenwander, D.; Frömling, T.; Thaman, H. L.; Berendts, S.; Uecker, R.; Carter, W. C.; Chiang, Y. M. Mechanism of Lithium Metal Penetration through Inorganic Solid Electrolytes. *Adv. Energy Mater.* **2017**, *7*, 1701003. DOI: 10.1002/AENM.201701003.

(42) Tsai, C. L.; Roddatis, V.; Chandran, C. V.; Ma, Q.; Uhlenbruck, S.; Bram, M.; Heitjans, P.; Guillon, O. Li7La3Zr2O12 Interface Modification for Li Dendrite Prevention. *ACS Appl. Mater. Interfaces* **2016**, *8*, 10617-10626. DOI: 10.1021/acsami.6b00831.

(43) Aguesse, F.; Manalastas, W.; Buannic, L.; Del Amo, J. M. L.; Singh, G.; Llordés, A.; Kilner, J. Investigating the dendritic growth during full cell cycling of garnet electrolyte in direct contact with Li metal. *ACS Appl. Mater. Interfaces* **2017**, *9*, 3808-3816. DOI: 10.1021/acsami.6b13925.

(44) Han, F.; Westover, A. S.; Yue, J.; Fan, X.; Wang, F.; Chi, M.; Leonard, D. N.; Dudney, N. J.; Wang, H.; Wang, C. High electronic conductivity as the origin of lithium dendrite formation within solid electrolytes. *Nat. Energy* **2019**, *4*, 187-196. DOI: 10.1038/s41560-018-0312-z.

(45) Kinzer, B.; Davis, A. L.; Krauskopf, T.; Hartmann, H.; LePage, W. S.; Kazyak, E.; Janek, J.; Dasgupta, N. P.; Sakamoto, J. Operando analysis of the molten Li|LLZO interface: Understanding how the physical properties of Li affect the critical current density. *Matter* **2021**, *4*, 1947-1961. DOI: 10.1016/j.matt.2021.04.016.

(46) Zhang, Q.; Lu, Y.; Guo, W.; Shao, Y.; Liu, L.; Lu, J.; Rong, X.; Han, X.; Li, H.; Chen, L.; Hu, Y.-S. Hunting Sodium Dendrites in NASICON-Based Solid-State Electrolytes. *Energy Mater. Adv.* **2021**, *2021*, 1-10. DOI: 10.34133/2021/9870879.

(47) Golozar, M.; Paolella, A.; Demers, H.; Bessette, S.; Lagacé, M.; Bouchard, P.; Guerfi, A.; Gauvin, R.; Zaghib, K. In situ observation of solid electrolyte interphase evolution in a lithium metal battery. *Commun. Chem.* **2019**, *2*, 1-9. DOI: 10.1038/s42004-019-0234-0.

(48) Krauskopf, T.; Dippel, R.; Hartmann, H.; Peppler, K.; Mogwitz, B.; Richter, F. H.; Zeier, W. G.; Janek, J. Lithium-Metal Growth Kinetics on LLZO Garnet-Type Solid Electrolytes. *Joule* **2019**, *3*, 2030-2049. DOI: 10.1016/J.JOULE.2019.06.013.

(49) Rees, G. J.; Spencer Jolly, D.; Ning, Z.; Marrow, T. J.; Pavlovskaya, G. E.; Bruce, P. G. Imaging Sodium Dendrite Growth in All-Solid-State Sodium Batteries Using 23Na T

2-Weighted Magnetic Resonance Imaging. *Angew. Chem. Int. Ed.* **2021**, *60*, 2110. DOI: 10.1002/ANIE.202013066.

(50) Shen, F.; Dixit, M. B.; Xiao, X.; Hatzell, K. B. Effect of Pore Connectivity on Li Dendrite Propagation within LLZO Electrolytes Observed with Synchrotron X-ray Tomography. *ACS Energy Lett.* **2018**, *3*, 1056-1061. DOI: 10.1021/ACSENERGYLETT.8B00249/SUPPL_FILE/NZ8B00249_SI_001.PDF.

(51) Su, H.; Zhang, S.-W.; Liu, Y.-M.; Yang, C.; Zhang, L.-X.; Xin, S.; You, Y. Na3Zr2Si2PO12 solid-state electrolyte with glass-like morphology for enhanced dendrite suppression. *Rare Met.* **2022**, *41* (12), 4086-4093. DOI: 10.1007/s12598-022-02161-4.

(52) Li, C.; Li, R.; Liu, K.; Si, R.; Zhang, Z.; Hu, Y. S. NaSICON: A promising solid electrolyte for solid-state sodium batteries. *Interdisciplinary Materials* **2022**, *1* (3), 396-416. DOI: 10.1002/idm2.12044.

(53) Gross, M. M.; Small, L. J.; Peretti, A. S.; Percival, S. J.; Rodriguez, M. A.; Spoerke, E. D. Tin-based ionic chaperone phases to improve low temperature molten sodium-NaSICON interfaces. *J. Mater. Chem. A* **2020**, *8*, 17012-17018. DOI: 10.1039/d0ta03571h.

(54) Park, H.; Jung, K.; Nezafati, M.; Kim, C. S.; Kang, B. Sodium Ion Diffusion in Nasicon (Na3Zr2Si2PO12) Solid Electrolytes: Effects of Excess Sodium. *ACS Appl. Mater. Interfaces* **2016**, *8*, 27814-27824. DOI: 10.1021/acsami.6b09992.

(55) Landmann, D.; Graeber, G.; Heinz, M. V. F.; Haussener, S.; Battaglia, C. Sodium plating and stripping from Na-β"-alumina ceramics beyond 1000 mA/cm2. *Mater. Today Energy* **2020**, *18*, 100515. DOI: 10.1016/J.MTENER.2020.100515.

(56) Chen, K. H.; Wood, K. N.; Kazyak, E.; Lepage, W. S.; Davis, A. L.; Sanchez, A. J.; Dasgupta, N. P. Dead lithium: Mass transport effects on voltage, capacity, and failure of lithium metal anodes. *J. Mater. Chem. A* **2017**, *5*, 11671-11681. DOI: 10.1039/C7TA00371D.

(57) Zhang, X.; Sahraei, E.; Wang, K. Li-ion Battery Separators, Mechanical Integrity and Failure Mechanisms Leading to Soft and Hard Internal Shorts. *Sci. Rep.* **2016**, *6* (1), 32578. DOI: 10.1038/srep32578.

(58) Wang, C.; Sun, Z.; Zhao, Y.; Wang, B.; Shao, C.; Sun, C.; Zhao, Y.; Li, J.; Jin, H.; Qu, L. Grain Boundary Design of Solid Electrolyte Actualizing Stable All-Solid-State Sodium Batteries. *Small* **2021**, *17*, 2103819-2103827. DOI: 10.1002/smll.202103819.

(59) Hongahally Basappa, R.; Ito, T.; Morimura, T.; Bekarevich, R.; Mitsuishi, K.; Yamada, H. Grain boundary modification to suppress lithium penetration through garnet-type solid electrolyte. *J. Power Sources* **2017**, *363*, 145-152. DOI: 10.1016/J.JPOWSOUR.2017.07.088.

(60) Yu, S.; Siegel, D. J. Grain Boundary Softening: A Potential Mechanism for Lithium Metal Penetration through Stiff Solid Electrolytes. *ACS Appl. Mater. Interfaces* **2018**, *10*, 48. DOI: 10.1021/acsami.8b17223.

(61) Freedman, J. F.; Robertson, W. D. Electrical Resistivity of Liquid Sodium, Liquid Lithium, and Dilute Liquid Sodium Solutions. *J. Chem. Phys.* **2004**, *34*, 769. DOI: 10.1063/1.1731673.

(62) Kazyak, E.; Garcia-Mendez, R.; LePage, W. S.; Sharafi, A.; Davis, A. L.; Sanchez, A. J.; Chen, K. H.; Haslam, C.; Sakamoto, J.; Dasgupta, N. P. Li Penetration in Ceramic Solid Electrolytes: Operando Microscopy Analysis of Morphology, Propagation, and Reversibility. *Matter* **2020**, *2*, 1025-1048. DOI: 10.1016/J.MATT.2020.02.008.

(63) Tu, Q.; Shi, T.; Chakravarthy, S.; Ceder, G. Understanding metal propagation in solid electrolytes due to mixed ionic-electronic conduction. *Matter* **2021**, *4*, 3248-3268. DOI: 10.1016/J.MATT.2021.08.004.

(64) Wood, K. N.; Kazyak, E.; Chadwick, A. F.; Chen, K.-H.; Zhang, J.-G.; Thornton, K.; Dasgupta, N. P. Dendrites and Pits: Untangling the Complex Behavior of Lithium Metal Anodes through Operando Video Microscopy. *ACS Cent. Sci.* **2016**, *2* (11), 790-801. DOI: 10.1021/acscentsci.6b00260.

Supporting Information

Molten Sodium Penetration in NaSICON Electrolytes at 0.1 A cm^{-2}

Ryan Hill,[a*] Amanda Peretti,[b] Leo J. Small,[b] Erik D. Spoerke,[b] and Yang-Tse Cheng[a]

a. Department of Chemical and Materials Engineering, University of Kentucky, Lexington, KY, 40506, USA

b. Sandia National Laboratories, Albuquerque, NM, 87123, USA

*Corresponding Author:
Ryan Hill
Department of Chemical and Materials Engineering
University of Kentucky College of Engineering
177 F Paul Anderson Tower
512 Administration Drive
Lexington, KY 40506
Ryan.C.Hill@uky.edu

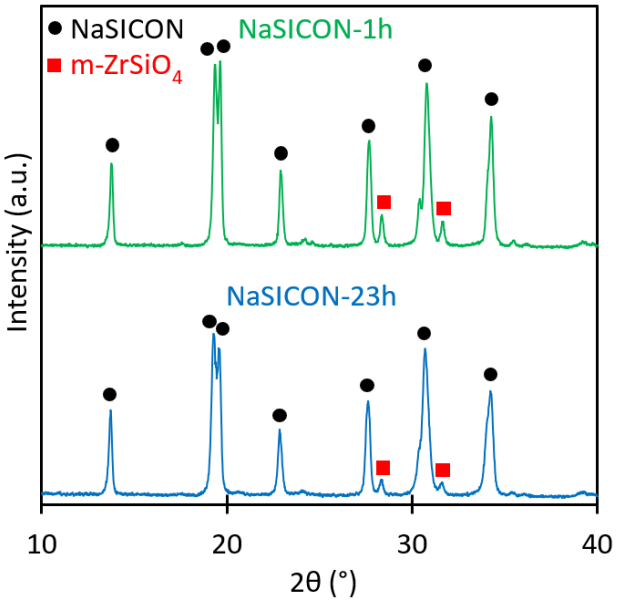

Figure S1. XRD patterns for pellets used in NaSICON-23h and NaSICON-1h cells. NaSICON and additional phase peaks are labeled accordingly.

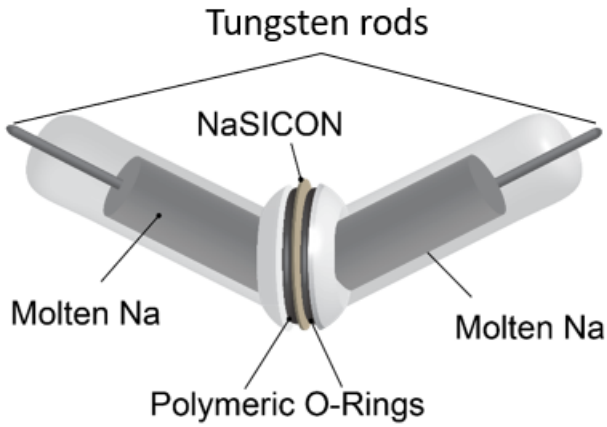

Figure S2. Schematic of Na|NaSICON|Na symmetric cells.

Table S1. Fitted EIS values for NaSICON-1h cell before and after constant current testing.

NaSICON-1h											
	L1 (H)	dev	R1 (Ω)	dev	R2 (Ω)	dev	a2	dev	Q2 ($F*s^{a2-1}$)	dev	Area Specific Resistance ($Ω*cm^2$)
Before Testing	3.0E-06	1.9E-07	2.7	1.1	16.1	0.9	0.82	0.60	6.3E-06	4.1E-06	33.2
After 1	2.8E-06	2.2E-07	2.5	1.5	9.8	1.4	0.79	0.66	1.2E-05	1.4E-05	21.8

Table S2. Fitted EIS values for NaSICON-23h cell before and after each constant current interval.

NaSICON-23h											
	L1 (H)	dev	R1 (Ω)	dev	R2 (Ω)	dev	a2	dev	Q2 ($F*s^{a2-1}$)	dev	Area Specific Resistance ($Ω*cm^2$)
Before Testing	3.0E-06	1.6E-07	2.0	0.9	18.7	0.8	0.83	0.59	4.0E-06	2.2E-06	36.4
After 1	2.9E-06	1.4E-07	2.2	1.2	12.0	1.0	0.81	0.64	8.9E-03	8.0E-06	24.9
After 2	2.8E-06	2.6E-07	2.3	0.9	15.9	0.8	0.82	0.61	7.1E-06	4.6E-06	32.1
After 3	2.8E-06	2.6E-07	2.6	0.8	16.2	0.6	0.82	0.60	7.0E-06	4.3E-06	33.2
After 4	2.9E-06	9.3E-07	3.0	2.6	6.0	2.6	0.81	0.76	1.1E-05	2.6E-05	15.8
After 5	2.7E-06	2.2E-07	2.9	1.0	14.4	0.9	0.80	0.61	8.5E-06	6.1E-06	30.5
After 6	2.8E-06	5.1E-07	2.4	1.9	8.2	1.8	0.80	0.70	1.0E-05	1.5E-05	18.7
After 7	2.8E-06	8.6E-07	2.3	2.7	6.2	2.6	0.79	0.75	1.3E-05	3.0E-05	14.9
After 8	2.9E-06	9.5E-07	2.5	2.8	6.1	2.7	0.79	0.75	1.3E-05	2.9E-05	15.1
After 9	3.1E-06	1.1E-06	2.5	3.1	5.1	3.0	0.81	0.79	1.1E-05	3.2E-05	13.3
After 10	2.8E-06	5.5E-07	2.3	2.1	7.1	2.1	0.80	0.72	9.6E-06	1.7E-05	16.6
After 11	2.9E-06	5.5E-07	2.3	2.0	7.0	2.0	0.81	0.73	9.4E-06	1.7E-05	16.2
After 12	2.9E-06	8.3E-07	2.1	2.6	5.8	2.5	0.80	0.76	1.1E-05	2.6E-05	13.9
After 13	2.9E-06	8.0E-07	2.1	2.6	5.7	2.5	0.81	0.77	1.1E-05	2.6E-05	13.7
After 14	3.0E-06	8.3E-07	2.1	2.7	5.4	2.6	0.81	0.78	9.9E-06	2.6E-05	13.1
After 15	2.9E-06	8.2E-07	2.0	2.7	5.6	2.6	0.81	0.77	1.0E-05	2.5E-05	13.4
After 16	2.9E-06	6.2E-07	2.6	2.3	6.9	2.2	0.79	0.72	1.2E-05	2.4E-05	16.7
After 17	2.9E-06	6.2E-07	2.8	2.3	6.6	2.3	0.81	0.73	8.9E-06	1.8E-05	16.5
After 18	3.0E-06	7.8E-07	2.7	2.7	6.2	2.7	0.80	0.74	9.5E-06	2.1E-05	15.7
After 19	2.9E-06	1.0E-06	3.9	3.2	5.1	3.2	0.81	0.79	8.9E+06	2.6E-05	15.8
After 20	2.9E-06	1.4E-06	3.4	4.1	4.1	4.1	0.81	0.82	8.8E-06	3.7E-05	13.3
After 21	2.9E-06	8.3E-07	2.7	2.8	7.0	2.7	0.81	0.72	7.8E-06	1.6E-05	17.0
After 22	2.9E-06	1.7E-06	2.1	4.6	3.5	4.6	0.81	0.86	9.9E-06	5.3E-05	9.8

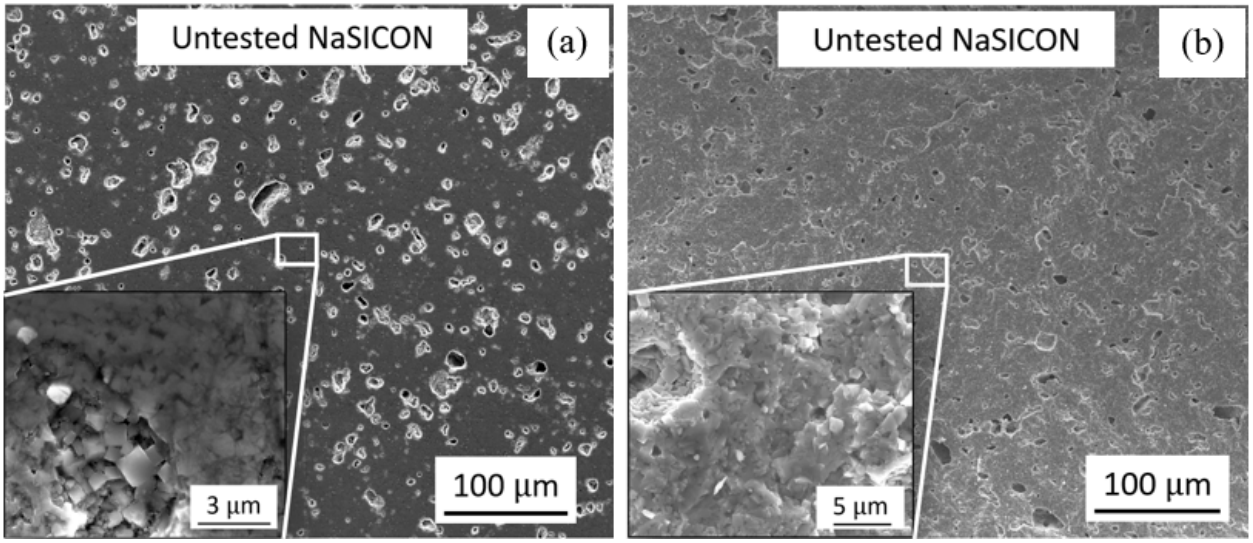

Figure S3. SEM images of NaSICON (a) surface and (b) cross section. Insets show a higher magnification of boxed region.

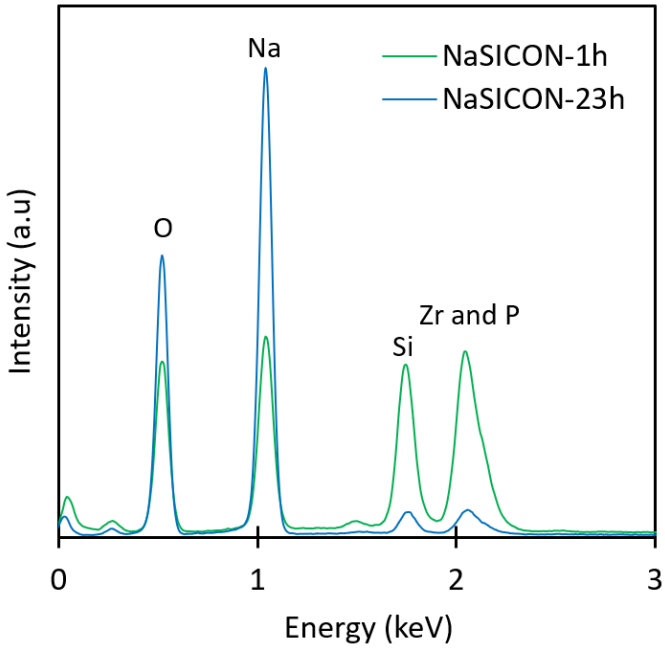

Figure S4. EDS spectra showing relevant elements for maps shown in **Figure 3** in main text showing relative intensity of each element in mapped regions.

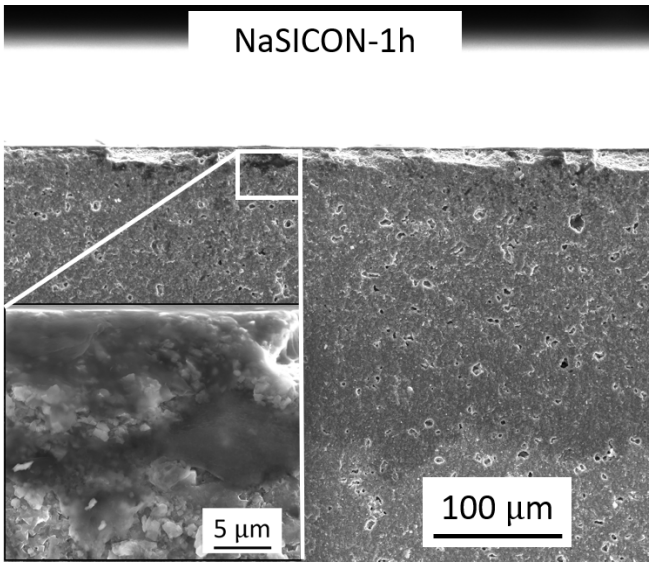

Figure S5. Cross-sectional SEM image of NaSICON-1h sample after testing. Inset shows a higher magnification of boxed region.

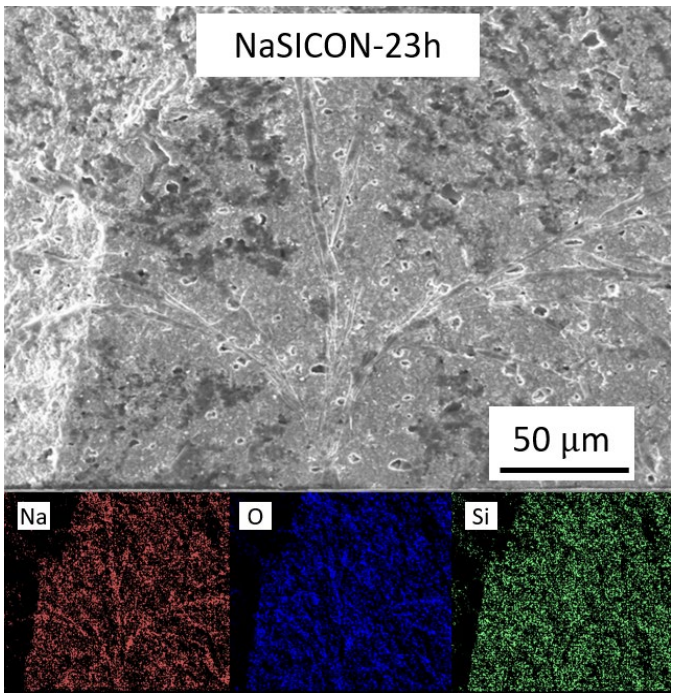

Figure S6. Cross-sectional SEM image and corresponding sodium, oxygen, and silicon EDS maps of NaSICON-23h sample after testing. The top of the image corresponds to the plating side of the electrolyte and the bottom of the image corresponds to the stripping side. A height difference on the left side of the image caused signal loss during the EDS scan.